ADVANCED MATERIALS
www.advmat.de

Beyond Human Touch Perception: An Adaptive Robotic Skin Based on Gallium Microgranules for Pressure Sensory Augmentation

*Simok Lee, Sang-Hyuk Byun, Choong Yeon Kim, Sungwoo Cho, Steve Park, Joo Yong Sim, and Jae-Woong Jeong**

Robotic skin with human-skin-like sensing ability holds immense potential in various fields such as robotics, prosthetics, healthcare, and industries. To catch up with human skin, numerous studies are underway on pressure sensors integrated on robotic skin to improve the sensitivity and detection range. However, due to the trade-off between them, existing pressure sensors have achieved only a single aspect, either high sensitivity or wide bandwidth. Here, an adaptive robotic skin is proposed that has both high sensitivity and broad bandwidth with an augmented pressure sensing ability beyond the human skin. A key for the adaptive robotic skin is a tunable pressure sensor built with uniform gallium microgranules embedded in an elastomer, which provides large tuning of the sensitivity and the bandwidth, excellent sensor-to-sensor uniformity, and high reliability. Through the mode conversion based on the solid–liquid phase transition of gallium microgranules, the sensor provides 97% higher sensitivity (16.97 kPa^{-1}) in the soft mode and 262.5% wider bandwidth (≈1.45 MPa) in the rigid mode compared to the human skin. Successful demonstration of the adaptive robotic skin verifies its capabilities in sensing a wide spectrum of pressures ranging from subtle blood pulsation to body weight, suggesting broad use for various applications.

1. Introduction

Robotic skin that mimics human skin can play a vital role in areas of robotics, metaverse, and healthcare and offers an immense opportunity for the development of human–machine interfaces, artificial intelligence, and many others.[1–5] To realize this possibility, electronic skin (e-skin) technology has rapidly evolved to overcome the gap between artificial and natural human skin in terms of its mechanical properties and tactile functions. Various researches on e-skin have been carried out to not only obtain the flexibility,[6–10] stretchability,[11] and self-healing ability[12,13] of human skin, but also to implement tactile sensing abilities to detect stimuli such as pressure,[13,14] temperature,[13,15–17] and humidity.[13,18,19] However, while state-of-the-art e-skin technologies have nearly achieved many of human skin properties and capabilities,[20,21] pressure sensing ability, which is considered as one of the primary capabilities of the skin,[22] is still limited in achieving actual skin-like performance, represented by high sensitivity and wide dynamic range.

Pressure sensors based on various working mechanisms—capacitive-,[23–25] piezoresistive-,[26–28] piezoelectric-,[14,29,30] and triboelectric-types[31–33]—have been investigated to enhance the sensing capability of the e-skin. For example, researchers have succeeded in enhancing the performance of pressure sensors by integrating a micro-/nanofabricated internal geometric structure (e.g., pyramidal microstructure, dome, pillar, or wrinkle pattern,[19,34–36]), embedding easily deformable materials (e.g., silicone, polyacrylic ester, hydrogel, and biomaterials,[37–40]), or integrating nanomaterials in 3D structures.[10,41] With these efforts, pressure sensing e-skins have shown dramatic improvements in their sensitivity and bandwidth.[25–27,30,40] However, while both enhanced sensitivity and enlarged bandwidth are necessary to catch up with or overtake the sensing performance of human skin, current pressure sensors integrated on e-skins have reached the limit of achieving only a single aspect (i.e., either sensitivity or bandwidth) among those two requirements due to the trade-off relationship between them.[23–27,31,42] For example, state-of-the-art e-skins integrated with pressure

S. Lee, S.-H. Byun, C. Y. Kim, S. Cho
School of Electrical Engineering
Korea Advanced Institute of Science and Technology (KAIST)
Daejeon 34141, Republic of Korea
S. Park
Department of Materials Science and Engineering
Korea Advanced Institute of Science and Technology (KAIST)
Daejeon 34141, Republic of Korea
J. Y. Sim
Department of Mechanical Systems Engineering
Sookmyung Women's University
Seoul 04310, Republic of Korea
J.-W. Jeong
School of Electrical Engineering
Korea Advanced Institute of Science and Technology (KAIST)
KAIST Institute for Health Science and Technology
Daejeon 34141, Republic of Korea
E-mail: jjeong1@kaist.ac.kr

The ORCID identification number(s) for the author(s) of this article can be found under https://doi.org/10.1002/adma.202204805.

DOI: 10.1002/adma.202204805

sensors with high sensitivity (35–99.5 kPa^{-1})[24,26,30,33] have limited bandwidth (e.g., ≈2 kPa (capacitive-type,[24]), ≈0.009 kPa (piezoresistive- and piezoelectric-type,[26,30]), and ≈19.8 kPa (triboelectric-type[33])), which restricts their potential applications for sensing a large pressure. On the other hand, a large bandwidth of sensors (e.g., ≈145 kPa (capacitive-type,[43]), ≈550 kPa (piezoresistive and piezoelectric devices[28,44]), and ≈1 MPa (triboelectric sensor[45])) has been obtained at the expense of sensitivity. Although these pressure sensors may offer an optimized sensing capability required for specific purposes, the trade-off between sensitivity and bandwidth hinders their realization of the human-skin-like sensing ability, which limits applications.

Previous efforts tried to address this issue by integrating multiple pressure sensors with distinct sensitivities and bandwidths side-by-side on the e-skin.[46,47] However, this approach not only wastes the device space, but it also results in poor lateral sensing resolution due to the spatial distribution of different sensing units. Novel materials and unique structural designs can bring new opportunities for device development.[48,49] As an alternate solution, tunable pressure sensing schemes, which allow tuning of both sensitivity and bandwidth, have been investigated by incorporating novel materials in device design. For example, a capacitive-type tunable pressure sensor (TPS) was developed using a phase-change gel (PC-gel) as the dielectric layer.[50] The PC-gel converts between the soft state with high sensitivity (21 kPa^{-1}) and low bandwidth (≈2 Pa) and the rigid state with low sensitivity (0.42 kPa^{-1}) and broad bandwidth (≈350 kPa) by changing the effective modulus of PC-gel through the phase transition.[50] However, due to the low effective modulus of the gel itself even in the rigid state, PC-gel-based TPSs still suffer from limited bandwidth and poor mechanical robustness. The gallium-based TPS,[51] recently demonstrated by our group, solved the limited bandwidth issue of the aforementioned TPS by utilizing the phase changing nature of gallium, which offers large elastic modulus tuning through conversion between a liquid- ($E \approx 0$) and a solid-state ($E \approx 9.8$ GPa),[51,52] thereby achieving high repeatability, sufficiently high sensitivity (≈15.77 kPa^{-1}; soft mode), and enlarged bandwidth (≈1.0 MPa; rigid mode). Although it offers excellent tunability and sensing capability as a single sensor unit, enabling sensor-to-sensor uniformity is challenging owing to the fundamental limitation of the current fabrication method, which relies on shear mixing of gallium and elastomer.[53] The sensor-to-sensor homogeneity is important for robotic skin applications where large-scale sensor arrays are necessary to cover a large surface area of the robotic body. However, the shear mixing method results in highly varying gallium particle sizes and shapes in the devices, thereby leading to nonuniform sensor-to-sensor performance.

Here, we present TPSs with high device-to-device uniformity and highly variable sensitivity and bandwidth to implement a large-scale adaptive robotic skin with superior sensing performances to the human skin. The sensor is based on a gallium–elastomer composite with the inclusion of uniform gallium microgranules (GMs), which produces high sensor-to-sensor uniformity and reliability. Through mode conversion based on the solid–liquid phase transition of GMs, our sensor provides high sensitivity (16.97 kPa^{-1}) in the soft mode and wide bandwidth (≈1.45 MPa) in the rigid mode, allowing measurements of various pressures ranging from 3 Pa to 1.45 MPa adaptively. Compared to human skin, our TPSs provide sensing of 97% lower minimum detectable pressure and 262.5% higher maximum detectable pressure (the detection range of human skin is from 100 Pa to 400 kPa[54–56]). Consequently, our TPSs establish an adaptive robotic skin by overcoming the issues associated with the sensitivity/bandwidth trade-off relationship as well as manufacturing of highly uniform sensors. The robotic skin integrates multiple TPSs into a 2D array form and its tunable sensing characteristics enable us to demonstrate a wide variety of sensing applications. The following sections present the design, fabrication, and characterization of our TPSs, along with a proof-of-principle demonstration of real-time sensing of a wide range of pressure. Overall, the unique sensing capabilities of gallium-microgranule-based tunable pressure sensors (GM-TPSs) shown here open the door to adaptive robotic skin with augmented sensing ability surpassing that of the human skin.

2. Results and Discussion

2.1. Overview of the GM-TPS for an Adaptive Robotic Skin

Figure 1a illustrates the concept of our adaptive robotic skin in two convertible modes each with different pressure sensing abilities. The adaptive robotic skin is integrated with an array of TPSs, whose sensitivity and bandwidth can be easily adjusted through a temperature-dependent rigid–soft mode conversion. The rigid-mode sensor covers a wide range of pressures, while the soft-mode sensor provides high sensitivity with a relatively narrower detection range. The changeover between the two modes leads to different applications of our TPS in each mode. For example, our robotic skin can measure heavy loads such as the weight of an infant in the rigid mode and subtle physiological changes (e.g., blood pressure) in the soft mode.

The TPS, which is capacitive-type pressure sensor, employs gallium as the mode-convertible medium to promptly convert between the rigid and soft modes for the control of its sensitivity and the detection bandwidth (Figure 1b). Capacitive pressure sensors are widely used due to their simple fabrication, low power consumption, outstanding repeatability, and large-scale manufacturability,[1,4,57] compared to other types of sensors such as piezoresistive,[26–28,42] piezoelectric,[14,29,30,44] and triboelectric sensors.[31–33] As the capacitive sensor measures pressure with a capacitance value that is inversely proportional to the distance between two parallel electrodes, the properties of the medium between electrodes determine the characteristics of a pressure sensor. To make the sensor mode-convertible and tunable, we chose gallium (melting temperature: 29.76 °C) as a core material based on its temperature-dependent phase changing behavior between solid and liquid, and created a gallium–elastomer composite for the capacitor medium by encapsulating dense GMs with an elastomer (Figure 1b, bottom). Note that the GMs can be produced with exceptional uniformity (coefficient of variation (CV): 4.78%), thereby facilitating batch fabrication of large-scale pressure sensors with negligible device-to-device variations in terms of their sensing performance.

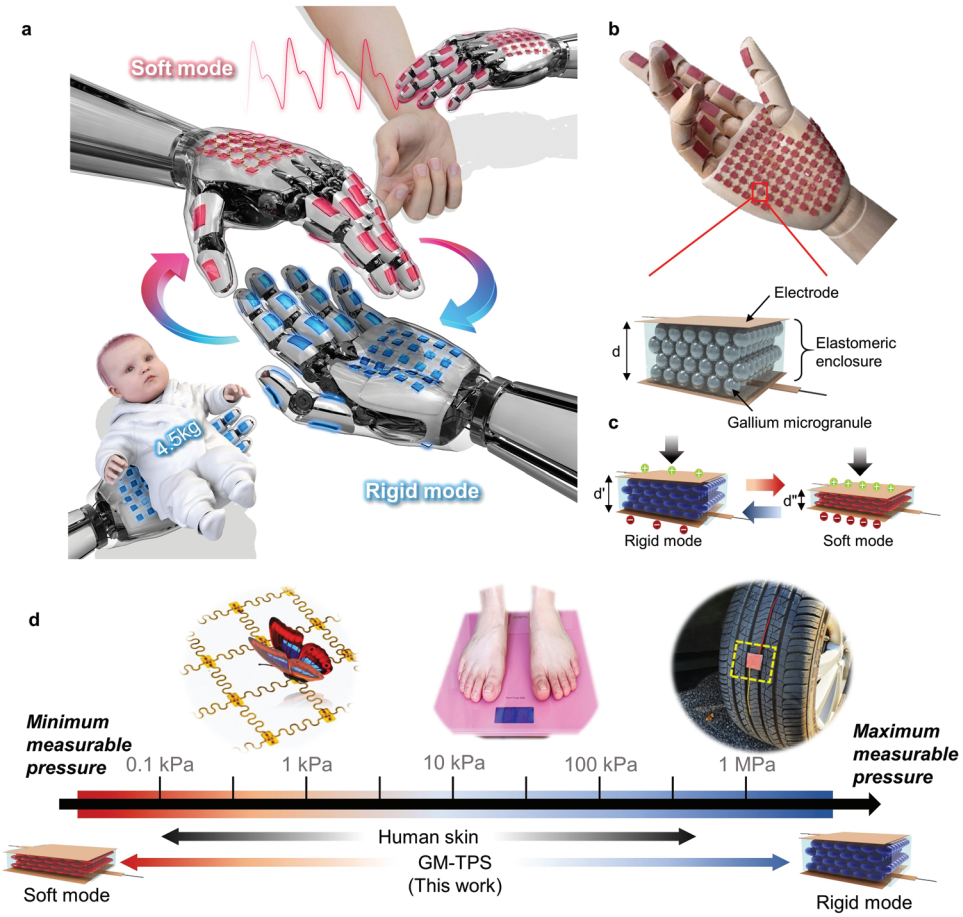

Figure 1. Overall concept and operation principle of an adaptive robotic skin integrated with arrays of TPSs, which dynamically adjust the sensitivity and dynamic range by converting between the rigid and soft modes based on the thermal response. a) Conceptual illustration of the adaptive robotic skin in two convertible modes with different pressure sensing abilities. The image shows potential application for nursing robots with ability to measure a wide range of body pressures. In the rigid mode, the robotic skin provides large bandwidth and can measure heavy loads, such as the weight of an infant. Switching to the soft mode offers high sensitivity, thereby enabling the detection of highly sophisticated pressures, such as those caused by physiological processes (e.g., blood pressure). b) Photograph of an adaptive robotic skin with an array of GM-TPSs, which are built using GMs encapsulated with elastomer. c) Schematic illustration revealing the sensing mechanism of the GM-TPSs that are convertible between the rigid (blue) and soft modes (red). In the rigid mode, solid GMs make the sensor less deformable under an applied pressure, resulting in a large bandwidth for pressure sensing. In the soft mode, liquid GMs make the sensor highly soft and deformable, leading to high sensitivity. d) Visualization of the sensing range of the adaptive robotic skin built with the GM-TPS, which surpasses the sensing ability of human skin. Compared to human skin, our GM-TPS can measure more subtle pressures in the soft mode and higher loads in the rigid mode.

Figure 1c exhibits the sensing mechanism of our GM-TPS in both the rigid and soft modes. The GM-TPS in each mode contains GMs in different phases—a solid phase in the rigid mode and a liquid phase in the soft mode—which show a distinct modulus that creates contrasting responses under external loads. The soft-mode sensor readily deforms its shape under pressure due to the low modulus (≈0 Pa) of liquified gallium, offering high sensitivity, while the rigid-mode sensor undergoes substantially smaller deformation due to the high modulus (9.8 GPa) of solidified GMs, thereby increasing the dynamic range of pressure sensing.

The GM-TPS exhibits sensing capabilities superior to that of the human skin. The pressure sensing ranges of the GM-TPS and human skin are compared in Figure 1d. Reportedly, human skin cannot detect pressure below 100 Pa and above 400 kPa[54–56] (e.g., <10 kPa for a gentle touch and 10–100 kPa for object manipulation[58]). Our GM-TPS overcomes this limitation, allowing measurement of pressures as low as 3 Pa (i.e., 97% lower than the lower limit of human skin bandwidth) and as high as 1.45 MPa (i.e., 262.5% higher than the upper limit of human skin bandwidth) through mode conversion between the soft and rigid modes. Due to the remarkable sensing ability of the GM-TPS, the adaptive robotic skin constructed with it opens numerous opportunities as demonstrated in our proof-of-concept experiments.

2.2. Device Fabrication and Systematic Study of Design Choices

2.2.1. Fabrication of the GM-TPS

The GM-TPS is manufactured by embedding gallium in a microgranular configuration with uniform size in an elastomer.

Unlike initial bulk state gallium, microgranular gallium suppresses its ductile nature and prevents a nonlinear sensing response, thus increasing repeatability and reliability of sensing capability.[51] To fabricate gallium in a microgranular structure, a T-junction microfluidic device is used to encapsulate the liquid gallium droplets with poly(dimethylsiloxane) (PDMS) solution. The immiscible PDMS solution injected from a continuous inlet stream encloses liquid gallium droplets injected from a discrete inlet stream, thereby monodispersing GMs to form GM–PDMS composites (**Figure 2**a). This novel method using a T-junction microfluidic system provides two key advantages for GM fabrication: it offers: i) easy control of the size and ii) uniform production of GMs. The diameter of the GMs can be controlled by varying several fabrication conditions, such as the ratio of the flow rates between the two inlet streams, the diameter of each inlet stream (Figure S1a, Supporting Information), and the velocity of the inlet stream while fixing the flow rate ratio (Figure S1b, Supporting Information). Among these conditions, altering the flow rate ratio has been shown to be the most simple and effective method to control the size of the GMs. The flow rate ratio of the PDMS to the gallium stream is adjusted to 27.85, 8.14, and 2.71, generating GMs with different diameters of 345 µm (size 1), 452 µm (size 2), and 883 µm (size 3), respectively, as shown in Figure 2b. Figure 2c shows the diameter distributions of the GMs in each GM–PDMS composite sample. It is necessary to make the GM size uniform during the fabrication process in order to ensure consistent sensor-to-sensor performance. In this regard, the characterization results in Figure 2c reveal that our microfluidic manufacturing approach has a clear advantage over the fabrication method based on manual shear mixing using a mortar and pestle.[51] The standard deviation of the GMs produced by the latter method is 227.1 µm (CV: 66.38%), whereas those of the GMs with size 1, 2, and 3 are only 15.4 µm (CV: 4.46%), 21.6 µm (CV: 4.78%), and 66.6 µm (CV: 7.54%), respectively, verifying highly uniform manufacturability of the microfluidic approach.

2.2.2. Systematic Study of Design Choices for the GM-TPS

In order to find the optimal design choice for the GM-TPS, three types of testbed sensors with different GM sizes (i.e., size 1, size 2, size 3) are fabricated with the same height (1 mm; Figure 1b, bottom), and their characteristics, such as sensitivity, hysteresis, and freezing temperature, are compared.

The sensitivity and hysteresis of each GM-TPS are obtained by measuring the relative capacitance changes under varying pressures in both the rigid mode (Figure 2d) and the soft mode (Figure 2e). The tangential slope on the plot represents sensitivity (Figure S2a, Supporting Information), and the quotient of the area inside the loop and the area below the loop of the curve represents hysteresis (Figure S2b, Supporting Information). Figure 2f shows the sensitivity of each GM-TPS when a pressure ranging from 0 to 1 kPa is applied. The rigid-mode sensors exhibit sensitivities of 2.04, 3.84, and 4.86 kPa^{-1} in sizes 1, 2, and 3, respectively, while the soft-mode sensors show substantially increased sensitivities of 8.53, 14.58, and 21.52 kPa^{-1}, respectively. The sensitivity of each sensor improves as the size of the embedded GMs increases because their larger size reduces the effective modulus of the entire sensor (Figure S3, Supporting Information). Moreover, our simulation (Figure S4, Supporting Information) demonstrates that our sensor undergoes larger deformation and has higher total strain energy under the same pressure as the size of the GMs increases, verifying that the effective modulus decreases as the gallium size increases according to the correlation between the total strain energy (U) and Young's modulus (E) (i.e., $U = \sigma^2 V / 2E$, where σ and V represent the stress and the volume of the sensor, respectively).

Hysteresis, which represents the difference in signals during loading and unloading, is another noteworthy metric used to compare the performance of pressure sensors. Low hysteresis enables accurate and repeatable sensing, which increases the reliability of the pressure sensor. Figure 2g shows the hysteresis of the GM-TPSs with GMs of different sizes in the soft and rigid modes. The loading and unloading speeds were fixed at 0.19 mm s^{-1} to minimize the effect of loading and unloading speed on the hysteresis (Figure S5, Supporting Information). Sensors with GMs of sizes 1, 2, and 3, respectively, show hysteresis of 1.49%, 2.71%, and 5.03%, in the soft mode and 6.10%, 9.01%, and 12.36% in the rigid mode. The GM-TPSs exhibit relatively low hysteresis compared to previous pressure sensors built with different materials (e.g., ≈13.29% for pure PDMS,[59] ≈38% for nanowire-coated tissue paper,[60,61] ≈45% for carbon-based cellular elastomers,[62] ≈11.5% for micropyramidal rubbers,[63] and ≈35% for hollow-sphered polypyrrole[64]). The low hysteresis stems from the microgranular structure of gallium that, compared to bulk gallium, possesses significantly lower ductility. However, even with a microgranular structure, solid gallium may not entirely lose its ductile nature, leading to the plastic deformation of the sensor under pressure. This problem is exacerbated as the size of the GM increases, thus resulting in increased hysteresis. This analysis is corroborated by the finite element analysis (FEA) simulation results that show the degree of plastic deformation of the GM-TPS (Figure S4c, Supporting Information). Another factor that induces hysteresis is the viscoelastic behavior of the elastomer.[65] The GM-TPS reduces the viscoelastic nature owing to its inclusion of an elastomer in a microporous form.[66] In this regard, sensors with smaller GMs contain the elastomer in a less clustered manner and thus exhibit lower hysteresis (Figure 2g).

Finally, we compare the freezing temperatures of the GMs of different sizes since they are directly related to the solid–liquid phase transition and thus the mode conversion of the GM-TPS. Here, we define the freezing temperature as the nucleation point, which is the temperature that initiates the phase transition. During the freezing process, gallium suffers from supercooling, a phenomenon in which the material maintains its liquid state at a temperature below its melting point until nucleation begins. Since the nucleation can be easily triggered in larger volumes,[67] small-sized gallium particles undergo severe supercooling issues and freeze at lower temperatures. The sensors with GMs of size 1, 2, and 3 have freezing temperatures of 19.42, 20.93, and 22.83 °C, respectively, when a cooling temperature of 0 °C is applied. This experimental result indicates that the operation mode of a sensor can be converted faster as the size of the GMs becomes larger (Figure 2h).

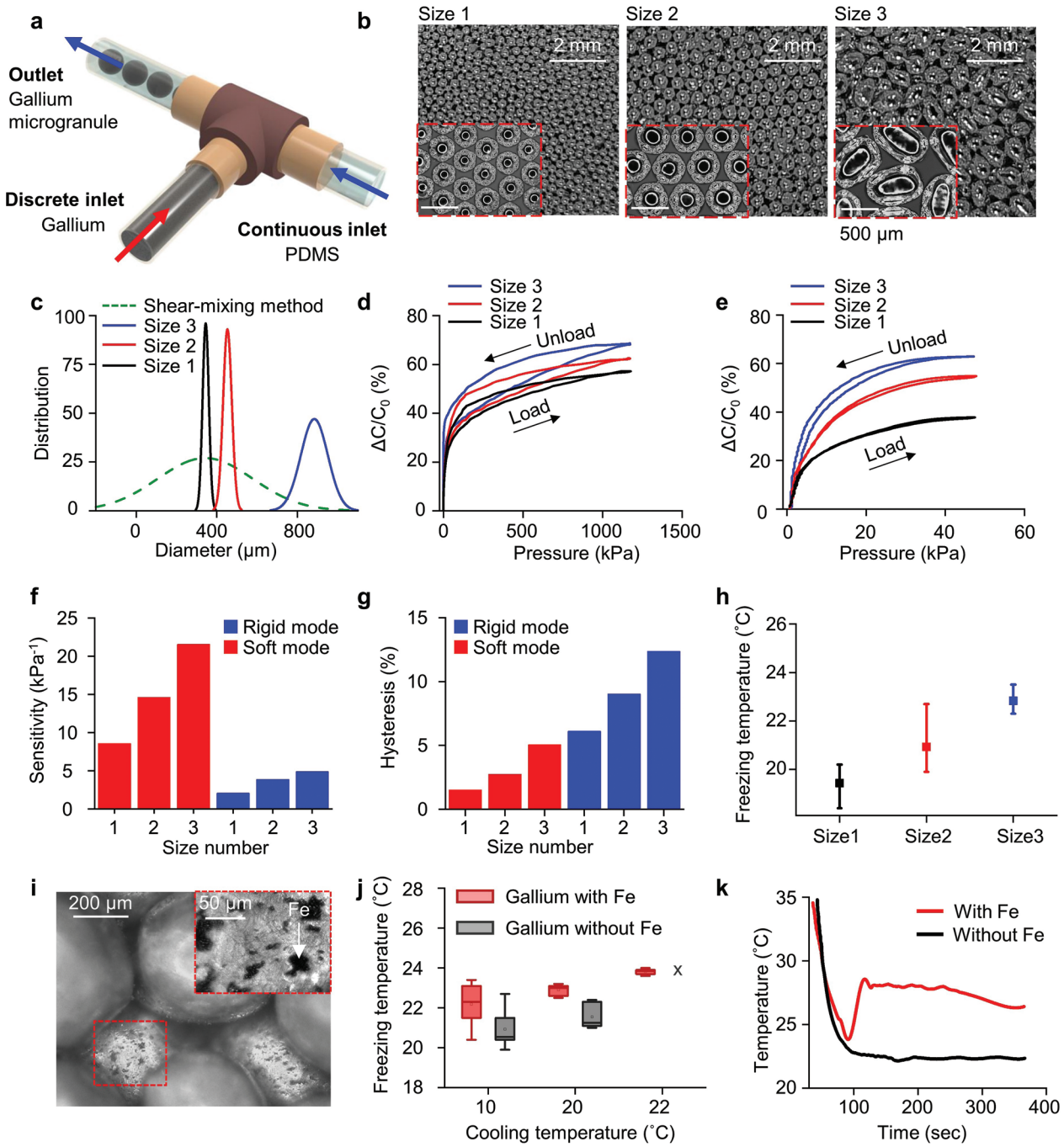

Figure 2. Systematic study on the design choices for the GM-TPS. a) Schematic diagram of a T-shaped microfluidic channel used for the fabrication of the GMs. The size of the GMs can be controlled by varying the flow rates of each inlet stream (continuous inlet: PDMS, discrete inlet: liquid gallium). b) Optical images of GMs of various sizes embedded in an elastomer (size 1: 345 μm, size 2: 452 μm, size 3: 883 μm). Each inset shows a microscopic view of each sample. Inset scale bars, 500 μm. c) Diameter distributions of GMs in various GM–PDMS composite samples. The green dotted line represents GMs manufactured by shear mixing, and three solid lines (black: size 1, red: size 2, blue: size 3) represent GMs fabricated using the microfluidics-based method shown in (a). d,e) Relative capacitance changes of GM-TPSs with GMs of different sizes (size 1, size 2, and size 3 in (b)) under applied pressure in the rigid (d) and soft modes (e). The GM-TPS is compressed up to 1.2 MPa and 50 kPa in the rigid and soft modes, respectively. Black, red, and blue lines represent plots for size 1, size 2, and size 3 in (b), respectively. f) Comparison of the sensitivity (in the pressure range of 0–1 kPa) and g) the hysteresis of the GM-TPSs with GMs of various sizes in the rigid (blue) and the soft (red) modes. h) Comparison of the freezing temperatures of GMs of different sizes (size 1, size 2, and size 3 in (b)) with an applied temperature of 0 °C. i) Optical microscopy image of GMs interfaced with iron (Fe) microparticles, which serve as nucleating agents that accelerate the mode switching by reducing the degree of supercooling during freezing of liquid gallium. The inset shows a magnified view of the area indicated by the red dotted box. j) Freezing temperatures of liquid GMs (size 2 in (b)) with and without the Fe additives. k) Plot comparing the temperature changes of GMs (size 2 in (b)) with (red) and without Fe additives (black) on a cooling temperature of 22 °C. Nucleation of Fe-added liquid gallium is triggered at 23.7 °C for solidification, but gallium without Fe additives remains supercooled, corroborating the catalytic effect of Fe additives on the solidification of liquid gallium during the freezing process.

Given these characteristics, GMs of size 2 (i.e., 452 µm) show superior features to other size options, allowing the GM-TPS to provide relatively high sensitivity, low hysteresis, and high freezing temperature with faster mode conversion, all of which are essential for an ideal TPS.

2.2.3. Improving the Mode Convertibility of GM-TPS

A GM-TPS fabricated with GMs of the selected size (size 2) still faces the supercooling problem, which limits the mode conversion speed. This problem can be alleviated through the addition of a nucleation agent.[68] Based on previous studies, which used metal powders as nucleation agents,[69,70] we added titanium carbide (TiC) and iron (Fe) to GMs during the fabrication process in order to accelerate the bidirectional mode conversion of the GM-TPS. Fe-added GMs, shown in Figure 2i, exhibit a remarkably reduced degree of supercooling, while TiC-added GMs only slightly decrease the degree of supercooling (Figure S6a, Supporting Information). Based on this experimental result, we use Fe microparticles as a nucleation agent. However, due to the large surface tension of gallium,[71] Fe microparticles are often distributed unevenly on the gallium surface and thus suppress supercooling inconsistently. To evenly distribute Fe microparticles on the surface of GMs, we mix Fe microparticles with a silicone elastomer and then transfer the composite to the surface of the GMs (Figure S6b,c, Supporting Information).

Figure 2j shows that Fe-added GMs can initiate a liquid-to-solid phase transition at higher temperatures due to the reduced degree of supercooling caused by Fe additives. When the cooling temperatures of the samples are 10 and 20 °C, the freezing points of Fe-added gallium increase by 1.35 and 1.25 °C, respectively, compared to those of pure gallium. Moreover, at the cooling temperature of 22 °C, only Fe-added GMs convert into the solid state (the initiating temperature is 23.85 °C), while pure GMs remain supercooled, confirming the catalytic effect of Fe additives on the solidification of liquid gallium during the cooling process (Figure 2k). Based on this, we used GMs of size 2 with Fe additives to develop high-performance GM-TPS for adaptive robotic skin.

2.3. Development and Performance Validation of the GM-TPS for Adaptive Robotic Skin

To enable the robotic skin to have sensing ability beyond the one of the human skin, the sensitivity and bandwidth of the pressure sensor need to be maximized. With this goal, we developed a GM-TPS with four layers of Fe-added microgranular gallium (size 2, 452 µm). Stacking four layers of the GM–PDMS composite improved the sensitivity and the dynamic range of the sensor (Figure S7, Supporting Information). The detailed fabrication process of the GM-TPS is presented in the Experimental Section. **Figure 3**a shows two distinct mechanical modes of the GM-TPS under compression. At each mode, a different state of the GMs (i.e., either solid or liquid) creates distinct responses of the sensor. The rigid-mode sensor is minimally deformed since the solid GMs undergo negligible distortion. The mechanical properties of the encapsulating PDMS which is softer than the solid GMs mainly determine the amount of deformation in rigid-mode sensor. Meanwhile, the soft-mode sensor is fully squashed due to the freely deformable nature of liquid GMs. Experimental measurement and FEA simulation (Figure 3b–d) show that the effective modulus of the sensor in the soft and rigid modes is 22.07 kPa and 13.5 MPa, respectively, offering a high tuning ratio of 612. Note that Figure 3d presents the pressure–strain curves, whose tangential slope represents the effective modulus.

The tunable nature of the sensor's mechanical property enables flexibility in sensing characteristics, including the sensitivity, dynamic range, and maximum withstandable pressure limit (Figure 3e). The sensitivity of our sensor can be tuned from 16.97 kPa^{-1} (soft mode) to 3.63 kPa^{-1} (rigid mode) in the 0–1 kPa range. Meanwhile, the mode conversion expands the dynamic range (i.e., the amount of pressure required to change the onset sensitivity by 1%) by 17.5 times from 80 kPa (soft mode) to 1.45 MPa (rigid mode). Moreover, the maximum withstandable pressure limits (i.e., yield strength, the amount of pressure that the sensor can endure without permanent change) are 460 kPa in the soft mode and 7.43 MPa in the rigid mode (Figure S8, Supporting Information). Considering that the pressure applied by a moving motorcycle (weighing about 170 kg) is 3.5 MPa,[72] it is obvious that our tunable sensor is mechanically robust. Our GM-TPS achieves significantly higher sensitivity and a broader dynamic range through mode conversion, compared to state-of-the-art capacitive sensors with a dynamic range of larger than 3 kPa (Figure 3f).[23,58,64,72–88] In the soft mode, the sensor has sensitivity of 16.97 kPa^{-1} within 0–1 kPa, 7.57 kPa^{-1} within 1–5 kPa, 2.47 kPa^{-1} within 5–10 kPa, 1.42 kPa^{-1} within 10–20 kPa, and 0.31 kPa^{-1} within 20–50 kPa. This result reveals that compared to reported contemporary sensors, our sensor has significantly higher sensitivity in the lower pressure range of 0–10 kPa, especially achieving a 452% improvement over the highest sensitivity of the state-of-the-art sensors (3.13 kPa^{-1}) in the 0–1 kPa range.[77] On the other hand, in the rigid mode, our sensor has a much wider bandwidth (1.45 MPa) than most existing sensors while maintaining higher sensitivity (0.02 kPa^{-1}) in the megapascal pressure range.

To verify the practicality and the reliability of our advanced sensor in the real world, it is necessary to validate its repeatability, response time, recovery time, and uniform manufacturability. Figure 3g,h, respectively, shows the stable operation of our GM-TPS in the rigid and soft modes over 4000 cycles of periodic loading–unloading with time-varying compressive stresses. For the cyclic test, the GM-TPS is pressed up to 1.2 MPa in the rigid mode and 49.1 kPa in the soft mode. The relative capacitance changes under repeated pressure are consistent through numerous cycles, showing high repeatability and reliability in both modes. Also, the GM-TPS shows consistent performance during the cyclic mode switching of GM-TPS, verifying the operational reliability of our robotic skin (Figure S9a–f, Supporting Information). Furthermore, the robust encapsulation of elastomer allows GM-TPS to be mechanically stable on different temperatures (Figure S9g, Supporting Information).[89] In addition, our sensor provides sufficiently fast response and recovery (Figure 3i,j) which is faster than the human's response time to a tactile stimulus (139 ms).[90] The response time, which is evaluated as an interval between 10% and 90% of relative

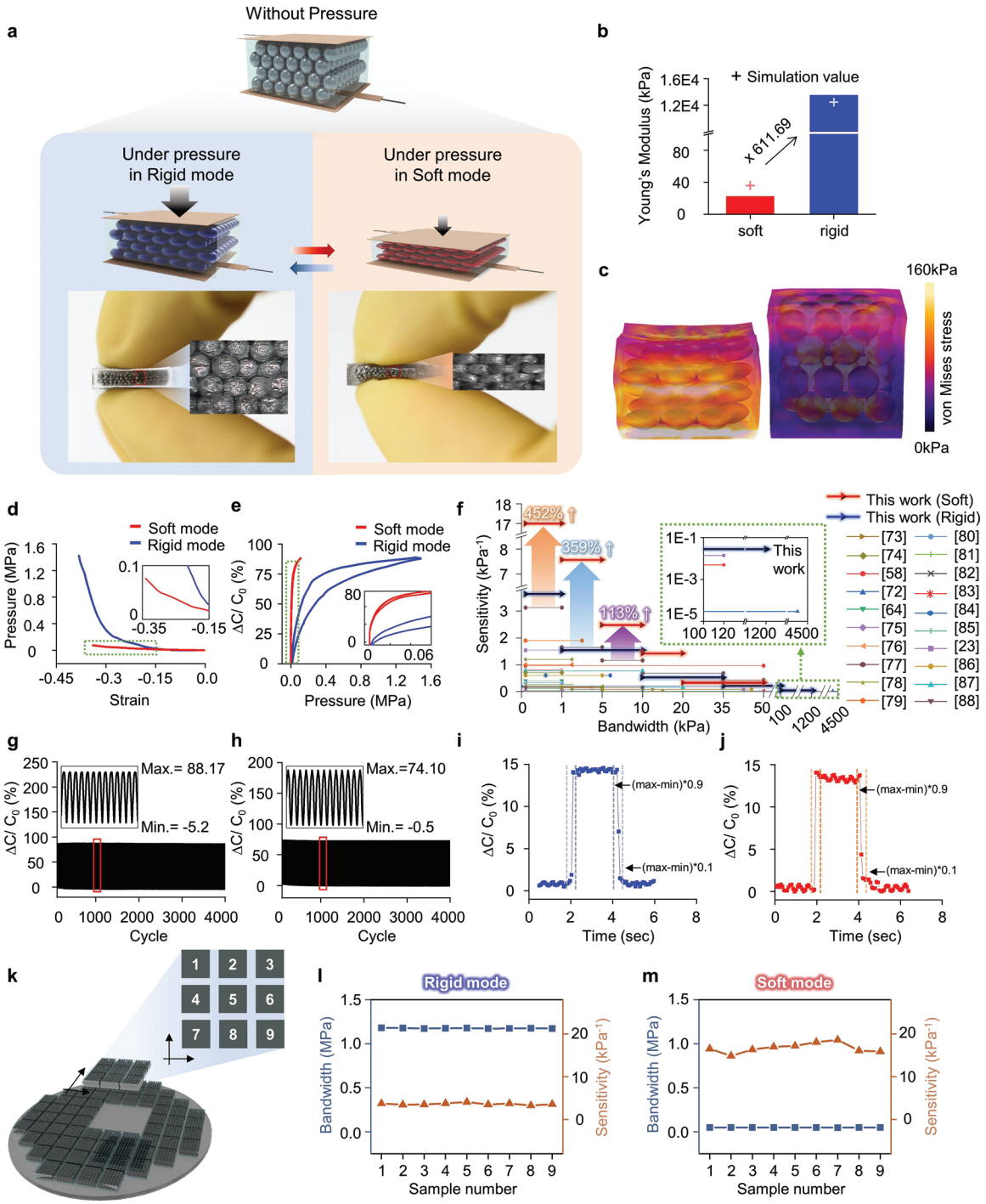

Figure 3. Characterization of the GM-TPS. a) Schematic illustration and optical images of the GM-TPS under pressure in the rigid and soft modes. The insets in the optical images show magnified views of the device cross-section in rigid and soft modes under compression. b) Plot showing change of the effective elastic modulus of the sensor in rigid and soft modes with the tuning ratio larger than 610. The symbol (+) indicates the effective modulus calculated through FEA simulation. c) FEA simulations exhibiting the von Mises stress distributions of the device under an applied pressure of 70 kPa in the soft mode (left) and the rigid mode (right). d) Pressure versus strain curves of the sensor in rigid (blue) and soft modes (red). The inset shows a magnified view of the graph for the pressure from 0 to 100 kPa. e) Relative capacitance changes versus pressure curves of the sensor in rigid (blue) and soft modes (red). The inset shows a magnified view of the graph for the pressure from 0 to 60 kPa. f) Comparison of the sensitivity and the bandwidth of our GM-TPS with state-of-the-art capacitive sensors in diverse pressure ranges. The inset with the green-dotted box shows a magnified view of the graph for the pressure range from 100 to 4500 kPa. g,h) Cyclic loading and unloading tests in the rigid (g) and soft modes (h) for 4000 cycles. The insets show magnified views of the graphs in the red boxed parts. i,j) Response and recovery times of the GM-TPS in the rigid (i) and soft modes (j). k) Schematic diagram illustrating the wafer-scale fabrication of the sensors. l,m) Plots illustrating the uniform bandwidths and the sensitivities of nine sensors from intrabatch (shown in (k)) in the rigid (l) and soft modes (m). In the rigid mode, a high effective modulus of the GM–PDMS composite leads to large bandwidth with low sensitivity. By contrast, in the soft mode, a low effective modulus of the composite produces substantially high sensitivity with a lower bandwidth.

capacitance changes under an abrupt application of pressure,[51] is 116 ms in the rigid mode and 58 ms in the soft mode. The recovery times are both 115 ms in the rigid and soft modes. The fast response and recovery times of the sensor make it suitable for dynamic sensing. For the response and recovery tests, the GM-TPS is pressed with stress of 45.9 kPa in the rigid mode and 300 Pa in the soft mode.

The homogeneity of GMs manufactured by a T-junction microfluidic system enables the consistency of the GM-TPS with uniform characteristics (i.e., bandwidth and sensitivity). We verify sensor-to-sensor uniformity by characterizing nine intrabatch sensors extracted from a single wafer-scale batch (4 in. wafer; Figure 3k and Figure S10a (Supporting Information)) and batch-to-batch uniformity by characterizing nine interbatch sensors equally extracted from a set of three batches (Figure S10b, Supporting Information). The bandwidth and sensitivity of the intrabatch sensors (Figure 3l,m) and interbatch sensors (Figure S10c,d, Supporting Information) are highly uniform with low standard deviations (CV for nine intrabatch sensors: 0.26% (bandwidth) and 6.54% (sensitivity) for the rigid mode, and 0.51% (bandwidth) and 6.82% (sensitivity) for the soft mode; similar values for the CV for nine interbatch sensors; Figure S10e,f, Supporting Information). The consistent sensing performance of the GM-TPS regardless of the fabricated batch and its location inside the batch promises uniform manufacturability over a large area, thus enabling sensor array fabrication for an adaptive robotic skin required to cover the robotic body with a large surface area.

2.4. Demonstrations of Adaptive Robotic Skin with Tunable Sensitivity and Bandwidth

The GM-TPS with tunable sensing performances and high uniformity enables the implementation of an adaptive robotic skin. **Figure 4** demonstrates an adaptive robotic skin with application scenarios that take advantage of both a wide dynamic range in the rigid mode and high sensitivity in the soft mode. The robotic skin consists of an array of the GM-TPSs (GM–PDMS composite with the integration of flexible electrodes at the top and bottom; 2 mm in thickness), an elastomeric enclosure (100 μm in thickness), and a microfluidic thermal actuator (1.7 mm in thickness) for active control of mode conversion (Figure 4a). This adaptive robotic skin is highly flexible to make conformal integration with curved surfaces (Figure S11, Supporting Information). The temperature of the sensor is controlled by injecting hot or cold water through the PDMS microfluidic channel of the thermal actuator (Video S1, Supporting Information). This active temperature control accelerates the solid–liquid phase transition of GMs to rapidly convert the robotic skin into a desirable operation mode. Figure 4b,c show the phase transition of GMs in the robotic skin when its temperature is shifted by the cold (3 °C) and hot (58 °C) water, respectively. During the rigid-mode conversion (cooling process; Figure 4b), the GMs in the robotic skin undergo a short supercooling state, and then become solid. It takes 49 s for liquid gallium to solidify (I*–III in Figure 4b). The states of I–I*, I*–II*, II*–III, and III–IV (Figure 4b, bottom) represent a liquid state, the supercooled state, phase transition, and a solid state of GMs, respectively. For the soft-mode conversion (thawing process; Figure 4c), hot water raises the temperature of the sensors causing the phase transition of solid GMs into a liquid state within 27 s (II–III in Figure 4c, bottom). The states of I–II, II–III, and III–IV (Figure 4c, bottom) represent a solid state, phase transition state, and liquid state of GMs, respectively. The phase transition time is directly related to the temperature of the water supplied (Figure S12, Supporting Information). Therefore, microfluidic thermal actuation with an appropriate water temperature can be utilized to further accelerate the mode conversion of the GM-TPS. The adaptive robotic skin can measure a wide range of pressure in different tasks, thanks to the high sensitivity and broad dynamic range of the GM-TPS. Since our adaptive robotic skin is built with single-type sensors, it brings many advantages—i) occupying less space for the sensing architecture, ii) avoiding the hassle of changing the sensor depending on applications, and iii) enhancing the reliability of the measurement.

Figure 4d depicts representative real-world applications of our robotic skin, allowing sensing of various degrees of pressure. For example, when used in human health monitoring, the adaptive robotic skin can convert between the soft and the rigid mode to sense physiological pressure ranging from a carotid artery pulse (≈10 kPa; soft mode) to the weight of an infant (≈600 kPa; rigid mode). Furthermore, our rigid-mode robotic skin is capable of measuring heavy loads, such as those induced by foot stepping and acupressure, while the soft-mode skin can detect subtle pressure, including ant movement (5.2 mg, corresponding to 3 Pa), the weight of a ladybug (70 mg, corresponding to 40 Pa), and waterdrops (25 mg per drop, corresponding to 14.4 Pa) (Figure 4d and Figure S13 (Supporting Information)).

Our measurement system connected with the adaptive robotic skin visualizes the sensing of applied pressure and provides real-time spatial pressure mapping using sensor arrays (Figure 4d, bottom and Videos S2–S4 (Supporting Information)). The spatial resolution of our sensor arrays is 1.8 mm, providing better sensing resolution than that of the human skin which is 2–3 mm at a fingertip and 7–10 mm at a palm.[91] The sensor arrays can measure spatial distribution of applied pressure, ranging from a large pressure (e.g., finger pressuring (Video S2, Supporting Information) and smashing with a hammer (Video S3, Supporting Information); rigid mode) to a light object placement (e.g., a universal serial bus (USB) flash drive (3 g) placement (Video S4, Supporting Information); soft mode)). The relative capacitance change (visualized with color bars in Figure 4d, bottom) to each action applying pressure corresponds to the response of our sensor array to the external load, where the reddish color indicates higher pressure. These proof-of-concept demonstrations with a wide range of pressure measurements verify versatility and practical utility of the adaptive robotic skin, opening opportunities for broad applications.

3. Conclusion

We have presented a novel adaptive robotic skin built with the GM-TPSs, which provide tunable bandwidth and sensitivity, device-to-device uniformity, and high reliability for pressure

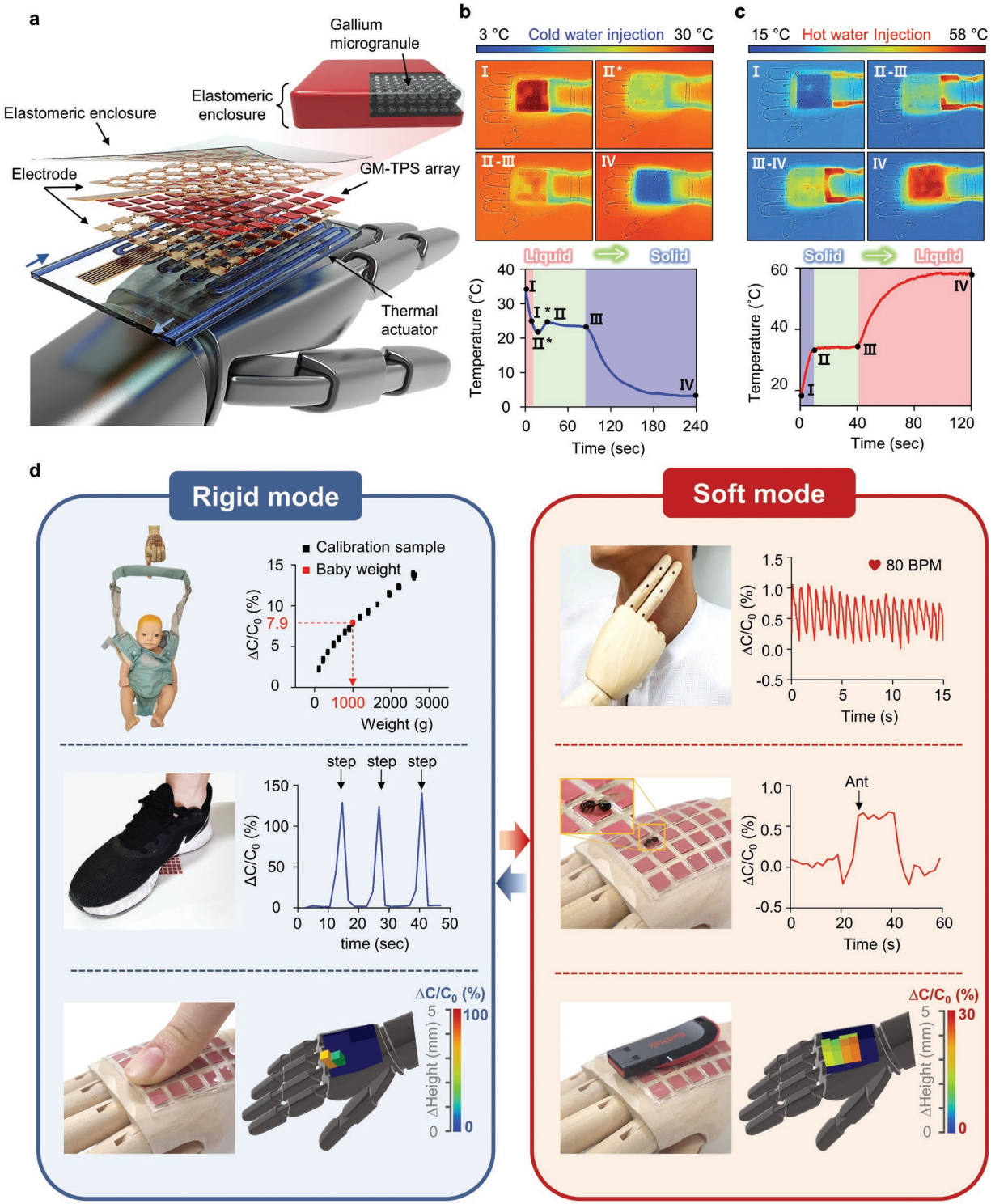

Figure 4. Application demonstration of an adaptive robotic skin with tunable pressure sensing ability. a) An exploded-view schematic diagram of an adaptive robotic skin comprised of five stacked layers with a zoom-in image of a single GM-TPS unit. The adaptive robotic skin consists of an array of uniform GM-TPSs with top and bottom flexible electrode layers and a microfluidic thermal actuator, which offers active temperature control that promotes solid–liquid phase transition of GMs. b,c) Infrared (IR) images and the corresponding phase transition plots of the robotic skin layer during soft-to-rigid conversion (b: freezing via cold water injection (3 °C)) and rigid-to-soft transition (c: thawing via hot water injection (58 °C)). In the plots, red, green, and blue shadings indicate a liquid state, liquid–solid (or solid–liquid) transition, and a solid state, respectively. d) Optical images and sensing plots of the adaptive robotic skin demonstrating its different pressure sensing abilities under two switchable rigid and soft modes. In the rigid mode (left), the robotic skin interface can measure large loads such as pressures induced by human weight, foot stepping, and acupressure. When converted to the soft mode, the robotic skin can sense subtle pressures such as those created by the carotid artery pulse, insect movements that correspond to a pressure of only 3 Pa, and the weight of a USB flash drive. The sensor array in both rigid and soft modes also provides spatial mapping of applied pressure as demonstrated in the bottommost applications.

sensing, enabling an augmented sensing beyond the human skin. The tunable nature of the integrated GM-TPSs, empowered by the solid–liquid phase transition of liquid metal gallium, enables swift mode conversion to promote a large bandwidth (1.45 MPa) in the rigid mode and ultrahigh sensitivity (16.97 kPa^{-1}) in the soft mode. Two main issues of gallium-based sensors—hysteresis and supercooling[51]—are addressed by building the sensors using uniform GMs created through a T-junction microfluidic system and integrating nucleation agents (i.e., Fe microparticles) with gallium, respectively. These approaches produce sensor-to-sensor uniformity and reproducibility, and facilitate the rapid mode conversion of the sensor by accelerating the liquid–solid phase change of gallium. Our proof-of-concept demonstration of a large-area adaptive robotic skin, composed of 2D arrays of these uniform GM-TPSs, verifies its unique sensing capability in measuring a wide spectrum of pressures with high spatial resolution, ranging from small-scale (e.g., carotid artery pulse, movement of ant, and water-drops) to large applied forces (e.g., the weight of an infant, foot stepping, and smashing with a hammer). With high versatility, uniformity, and reliability of the GM-TPS, we envision that the proposed adaptive robotic skin will lead to compelling outlooks in numerous applications, including nursing and assistive robotics, human–machine interfaces, metaverse realization, and many others.

4. Experimental Section

Fabrication of the GM-TPS: T-junction microfluidic device, comprised of a T-shape connecter (Tee assembly Tefzel (ethylene-tetrafluoroethylene (ETFE))), inner diameter is 1.27 mm) connected with three Tefzel (ETFE)-tube-based microfluidic channels (two inlet and one outlet channels; outer and inner diameter were 1.59 and 1.02 mm, respectively), was used to create a composite of GMs and elastomer. The silicone elastomer was prepared by mixing PDMS (SYLGARD 184, Dow Corning) with hexadecane (99%, Sigma-Aldrich) in a weight ratio of 1:1. The syringe containing PDMS solution was injected in the continuous inlet stream of the T-junction device while the syringe containing liquid gallium (Ga metal 99.99, Rich Metal) was injected in the discrete inlet stream. This led to production of uniform GMs encapsulated with elastomers, ejected through a single outlet stream. The size of GM was controlled by varying the flow rates of injection using the syringe pump (NEWERA). The flow rate ratio of the PDMS solution to the gallium stream was adjusted to 27.85, 8.14, and 2.71, while the speed of gallium inlet was fixed to 0.27 mL min^{-1}. These conditions allowed generation of GMs with different diameters of 345 µm (size 1), 452 µm (size 2), and 883 µm (size 3), respectively. The gallium–elastomer composite was accumulated in a wafer-scale plastic batch with a dimeter of 100 mm and cured at 70 °C for 1 day. For robust encapsulation, another silicone elastomer (RT 623 A/B, mixing ratio of 9:1, ELASTOSIL) was thinly spin-coated (200 µm) on the gallium–elastomer composite. Finally, the flexible electrodes—copper-coated polyimide film (18 µm, Q-Mantic; for single unit sensors) or a custom-designed flexible circuit board (copper-coated polyimide, 0.1 mm, PCBWay; for 2D array sensors)—were integrated at the top and bottom of the gallium–elastomer composite to complete a capacitive GM-TPS.

Integration of Nucleation Agents into GMs: Titanium carbide (≥99%, Sigma-Aldrich) and iron microparticles (≥99%, Sigma-Aldrich) were prepared and compared for the nucleation agents of gallium. Nucleation agents were mixed with silicone elastomer and injected in the continuous stream which was linked to the T-shape connector. While silicone elastomer encapsulated the GMs, the nucleation agents were transferred to the surface of GMs. Detailed experiment results can be found in Figure 2 and Figure S6 (Supporting Information).

Thermal Studies of the Phase-Change Behavior of the GM-TPS: To investigate the freezing point of the gallium–elastomer composites (Figure 2j), they were first thawed on the hot plate of 35 °C. Then, the soft composite with liquid gallium was moved to the cool plate (10, 20, 22 °C), and the phase-change behaviors of the gallium–elastomer composites were monitored and analyzed using an infrared (IR) camera (A655sc, FLIR). For the mode conversion of the adaptive robotic skin (Figure 4b,c), the sensor temperature was controlled by flowing hot (65 °C) or cold water (1 °C) into the microfluidic channel. Subsequently, the phase-change behaviors were captured using the IR camera and analyzed with FLIR program.

Characterization of the GM-TPS: The capacitance changes of the GM-TPS according to applied force were measured by an LCR meter (4284A Precision LCR Meter, Hewlett Packard, detection limit: 0.00001 pF) to study its characteristics. The absolute capacitance of the GM-TPS without pressure was 4.6 pF. The mechanical press machine (0.19 mm s^{-1}, Mark-10, ESM303) and a force gauge (Mark-10, Series-5) compressed the sensor. The LabVIEW software which was connected to an LCR meter, a press machine, and a force gauge showed the value of force, stain, and the capacitance changes. The applied force was divided by the contact area of the sensor to obtain the pressure. The dynamic range was obtained by calculating the amount of pressure required to lower the onset sensitivity by 1%. The effective modulus of the sensor was obtained by applying strain to the sensor, followed by analyzing the tangential slope of the stress versus strain curve.

Mechanical Modeling and Finite Element Analysis: A commercial FEA software (COMSOL Multiphysics, COMSOL, Inc.) was used to calculate the effective modulus of the sensor and analyze the sensor's response under compression. To compare the effective moduli of the sensors with different diameters, 3D models of sensors fabricated with GMs (Young's modulus of solid gallium = 9.8 GPa) of three different diameters (300, 450, and 900 µm) embedded in PDMS (Young's modulus of PDMS = 600 kPa) were prepared. The effective moduli were derived from total strain energy–pressure curves, when the sensors were pressed up to 80 kPa in the soft mode and 8 MPa in the rigid mode. Furthermore, to determine how the sensor reacted under the same pressure depending on its mode, 70 kPa was applied identically to sensors in different modes. The stress distribution under pressure was depicted by von Mises stress. Detailed experiment results can be found in Figure 3 and Figures S3 and S4 (Supporting Information).

Fabrication of the Adaptive Robotic Skin: The adaptive robotic skin consisted of a microfluidic thermal actuator, a 2D array of GM-TPSs, and an elastomeric enclosure. The microfluidic thermal actuator was built by bonding two different PDMS layers, one with a patterned fluidic channel and the other with flat layer. The flat PDMS layer (100 µm thickness) was prepared by spin-coating and cured at 70 °C for 60 min. The mold for the fluidic layer was made into the desired channel pattern using a 3D printer (Core 530, B9 Creations). The mold was pretreated with an antistiction spray (ER-200, Smooth-On) and PDMS was poured on the mold. After curing of PDMS at 70 °C for 60 min, the patterned PDMS was detached from the mold. Both PDMS layers underwent oxygen-plasma treatment (8 W for 5 min, Piezobrush PZ3, Relyon Plasma). The plasma treatment of PDMS exposed the silanol group to the surface of the PDMS, allowing formation of a strong covalent bond with other PDMS. To enhance its bonding, two attached PDMS layers were cured at 90 °C for 5 min. Then, a 2D array of GM-TPSs was integrated on the top of the microfluidic thermal actuator. Finally, thin PDMS layer (100 µm thickness) was applied to encapsulate the robotic skin for additional protection.

Real-Time Spatial Mapping of Applied Pressure for 3D Visualization: Two Arduino-based breakout boards (MPR121, Adafruit) were each connected to 8 different sensors on a 4 × 4 sensor array to record its sensing behavior in real time. MPR121 converted an analog signal, which was induced by applied pressure on the sensor array, to a digital signal represented as a 10-bit analog-to-digital conversion (ADC). Then, the relative capacitance was calculated from the 10-bit ADC counts based on the equation $C = (I \times T \times 1024) / (\text{ADC counts} \times V_{dd})$, where C is the capacitance value, I is the selected charge current (16 µA), T is the

selected charge time (1 ms), and V_{dd} is the power supply input (3.3 V). Then, the relative capacitance values were visualized through a 3D array spatial mapping (*x*- and *y*-axis: position of applied pressure, *z*-axis: magnitude of pressure) implemented in Python programming language.

Experiments on Human Subjects: All experiments on human skins were performed under approval from Institutional Review Board at Korea Advanced Institute of Science and Technology (protocol number: KH2018-35) and received informed consent from the volunteer subjects.

Statistical Analysis: Figure 2h,j contained plots ($n = 6$). The number of samples for Figure 3l,m and Figure S10c,d (Supporting Information) was 9. Figure S10e,f (Supporting Information) expressed means with standard deviations ($n = 9$). Figure S12a,b (Supporting Information) contained plots ($n = 5$). All data were processed with OriginLab.

Supporting Information

Supporting Information is available from the Wiley Online Library or from the author.

Acknowledgements

S.L. and S.-H.B. contributed equally to this work. This work was supported by the National Research Foundation of Korea (NRF-2022M3H4A1A02076825), Institute of Information & Communications Technology Planning & Evaluation (IITP-2022-0-00025) funded by the Ministry of Science and ICT, and an internal grant of Electronics and Telecommunications Research Institute (22RB1100, Exploratory and Strategic Research of ETRI-KAIST ICT Future Technology).

Conflict of Interest

The authors declare no conflict of interest.

Data Availability Statement

The data that support the findings of this study are available from the corresponding author upon reasonable request.

Keywords

gallium, robotic skins, sensory augmentation, stiffness tuning, tunable pressure sensors

Received: May 27, 2022
Revised: July 27, 2022
Published online:

[1] M. L. Hammock, A. Chortos, B. C.-K. Tee, J. B.-H. Tok, Z. Bao, *Adv. Mater.* **2013**, *25*, 5997.
[2] Y. H. Jung, B. Park, J. U. Kim, T. Kim, *Adv. Mater.* **2019**, *31*, 1803637.
[3] X. Wang, L. Dong, H. Zhang, R. Yu, C. Pan, Z. L. Wang, *Adv. Sci.* **2015**, *2*, 1500169.
[4] A. Chortos, J. Liu, Z. Bao, *Nat. Mater.* **2016**, *15*, 937.
[5] U. Pierre Claver, G. Zhao, *Adv. Eng. Mater.* **2021**, *23*, 2001187.
[6] E. Song, C. H. Chiang, R. Li, X. Jin, J. Zhao, M. Hill, Y. Xia, L. Li, Y. Huang, S. M. Won, K. J. Yu, X. Sheng, H. Fang, M. A. Alam, Y. Huang, J. Viventi, J. K. Chang, J. A. Rogers, *Proc. Natl. Acad. Sci. USA* **2019**, *116*, 15398.
[7] S. Gao, X. Zhao, Q. Fu, T. Zhang, J. Zhu, F. Hou, J. Ni, C. Zhu, T. Li, Y. Wang, V. Murugadoss, G. A. M. Mersal, M. M. Ibrahim, Z. M. El-Bahy, M. Huang, Z. Guo, *J. Mater. Sci. Technol.* **2022**, *126*, 152.
[8] G. Li, L. Wang, X. Lei, Z. Peng, T. Wan, S. Maganti, M. Huang, V. Murugadoss, I. Seok, Q. Jiang, D. Cui, A. Alhadhrami, M. M. Ibrahim, H. Wei, *Adv. Compos. Hybrid Mater.* **2022**, *5*, 853.
[9] Z. Zhang, M. Liu, M. M. Ibrahim, H. Wu, Y. Wu, Y. Li, G. A. M. Mersal, I. H. El Azab, S. M. El-Bahy, M. Huang, Y. Jiang, G. Liang, P. Xie, C. Liu, *Adv. Compos. Hybrid Mater.* **2022**, *5*, 1054.
[10] Y. Wu, J. Liu, S. Lin, K. Huang, E. Chen, K. Huang, M. Lei, *Eng. Sci.* **2022**, *18*, 105.
[11] D.-H. Kim, N. Lu, R. Ma, Y.-S. Kim, R.-H. Kim, S. Wang, J. Wu, S. M. Won, H. Tao, A. Islam, K. J. Yu, T. Kim, R. Chowdhury, M. Ying, L. Xu, M. Li, H.-J. Chung, H. Keum, M. McCormick, P. Liu, Y.-W. Zhang, F. G. Omenetto, Y. Huang, T. Coleman, J. A. Rogers, *Science* **2011**, *333*, 838.
[12] B. C.-K. Tee, C. Wang, R. Allen, Z. Bao, *Nat. Nanotechnol.* **2012**, *7*, 825.
[13] J. Chen, Y. Zhu, X. Chang, D. Pan, G. Song, Z. Guo, N. Naik, *Adv. Funct. Mater.* **2021**, *31*, 2104686.
[14] W. Navaraj, R. Dahiya, *Adv. Intell. Syst.* **2019**, *1*, 1900051.
[15] S. Y. Hong, Y. H. Lee, H. Park, S. W. Jin, Y. R. Jeong, J. Yun, I. You, G. Zi, J. S. Ha, *Adv. Mater.* **2016**, *28*, 930.
[16] Y. Hattori, L. Falgout, W. Lee, S.-Y. Jung, E. Poon, J. W. Lee, I. Na, A. Geisler, D. Sadhwani, Y. Zhang, Y. Su, X. Wang, Z. Liu, J. Xia, H. Cheng, R. C. Webb, A. P. Bonifas, P. Won, J.-W. Jeong, K.-I. Jang, Y. M. Song, B. Nardone, M. Nodzenski, J. A. Fan, Y. Huang, D. P. West, A. S. Paller, M. Alam, W.-H. Yeo, J. A. Rogers, *Adv. Healthcare Mater.* **2014**, *3*, 1597.
[17] N. Jiang, D. Hu, Y. Xu, J. Chen, X. Chang, Y. Zhu, Y. Li, Z. Guo, *Adv. Compos. Hybrid Mater.* **2021**, *4*, 574.
[18] L. Ma, R. Wu, A. Patil, S. Zhu, Z. Meng, H. Meng, C. Hou, Y. Zhang, Q. Liu, R. Yu, J. Wang, N. Lin, X. Y. Liu, *Adv. Funct. Mater.* **2019**, *29*, 1904549.
[19] L. Miao, J. Wan, Y. Song, H. Guo, H. Chen, X. Cheng, H. Zhang, *ACS Appl. Mater. Interfaces* **2019**, *11*, 39219.
[20] J.-W. Jeong, W.-H. Yeo, A. Akhtar, J. J. S. Norton, Y.-J. Kwack, S. Li, S.-Y. Jung, Y. Su, W. Lee, J. Xia, H. Cheng, Y. Huang, W.-S. Choi, T. Bretl, J. A. Rogers, *Adv. Mater.* **2013**, *25*, 6839.
[21] H.-R. Lim, H. S. Kim, R. Qazi, Y.-T. Kwon, J.-W. Jeong, W.-H. Yeo, *Adv. Mater.* **2020**, *32*, 1901924.
[22] F. Yin, J. Yang, H. Peng, W. Yuan, *J. Mater. Chem. C* **2018**, *6*, 6840.
[23] Y. Wan, Z. Qiu, J. Huang, J. Yang, Q. Wang, P. Lu, J. Yang, J. Zhang, S. Huang, Z. Wu, C. F. Guo, *Small* **2018**, *14*, 1801657.
[24] M. Pruvost, W. J. Smit, C. Monteux, P. Poulin, A. Colin, *npj Flexible Electron.* **2019**, *3*, 7.
[25] S. Chen, L. Sun, X. Zhou, Y. Guo, J. Song, S. Qian, Z. Liu, Q. Guan, E. Meade Jeffries, W. Liu, Y. Wang, C. He, Z. You, *Nat. Commun.* **2020**, *11*, 1107.
[26] Y. Gao, C. Yan, H. Huang, T. Yang, G. Tian, D. Xiong, N. Chen, X. Chu, S. Zhong, W. Deng, Y. Fang, W. Yang, *Adv. Funct. Mater.* **2020**, *30*, 1909603.
[27] Y. Guo, M. Zhong, Z. Fang, P. Wan, G. Yu, *Nano Lett.* **2019**, *19*, 1143.
[28] C. Liu, W. Zhu, M. Li, X. Sun, X. Guo, J. Liu, P. Liu, Y. Zhang, Y. Huang, *Org. Electron.* **2020**, *76*, 105447.
[29] B. Dutta, E. Kar, N. Bose, S. Mukherjee, *ACS Sustainable Chem. Eng.* **2018**, *6*, 10505.
[30] K. Maity, S. Garain, K. Henkel, D. Schmeißer, D. Mandal, *ACS Appl. Polym. Mater.* **2020**, *2*, 862.
[31] Z. Wen, Y. Yang, N. Sun, G. Li, Y. Liu, C. Chen, J. Shi, L. Xie, H. Jiang, D. Bao, Q. Zhuo, X. Sun, *Adv. Funct. Mater.* **2018**, *28*, 1803684.
[32] G. Yao, L. Xu, X. Cheng, Y. Li, X. Huang, W. Guo, S. Liu, Z. L. Wang, H. Wu, *Adv. Funct. Mater.* **2020**, *30*, 1907312.
[33] M. Ha, S. Lim, S. Cho, Y. Lee, S. Na, C. Baig, H. Ko, *ACS Nano* **2018**, *12*, 3964.

[34] S. H. Cho, S. W. Lee, S. Yu, H. Kim, S. Chang, D. Kang, I. Hwang, H. S. Kang, B. Jeong, E. H. Kim, S. M. Cho, K. L. Kim, H. Lee, W. Shim, C. Park, *ACS Appl. Mater. Interfaces* **2017**, *9*, 10128.
[35] C. Li, P.-M. Wu, S. Lee, A. Gorton, M. J. Schulz, C. H. Ahn, *J. Microelectromech. Syst.* **2008**, *17*, 334.
[36] P. Lu, L. Wang, P. Zhu, J. Huang, Y. Wang, N. Bai, Y. Wang, G. Li, J. Yang, K. Xie, J. Zhang, B. Yu, Y. Dai, C. F. Guo, *Sci. Bull.* **2021**, *66*, 1091.
[37] J. Park, J. Kim, J. Hong, H. Lee, Y. Lee, S. Cho, S.-W. Kim, J. J. Kim, S. Y. Kim, H. Ko, *NPG Asia Mater.* **2018**, *10*, 163.
[38] J. Mu, C. Hou, G. Wang, X. Wang, Q. Zhang, Y. Li, H. Wang, M. Zhu, *Adv. Mater.* **2016**, *28*, 9491.
[39] J. Duan, X. Liang, J. Guo, K. Zhu, L. Zhang, *Adv. Mater.* **2016**, *28*, 8037.
[40] Y. Hu, K. Qi, L. Chang, J. Liu, L. Yang, M. Huang, G. Wu, P. Lu, W. Chen, Y. Wu, *J. Mater. Chem. C* **2019**, *7*, 6879.
[41] Y. Wu, E. Chen, X. Weng, Z. He, G. Chang, X. Pan, J. Liu, K. Huang, K. Huang, M. Lei, *Eng. Sci.* **2022**, *18*, 113.
[42] C. Yang, L. Li, J. Zhao, J. Wang, J. Xie, Y. Cao, M. Xue, C. Lu, *ACS Appl. Mater. Interfaces* **2018**, *10*, 25811.
[43] W. Asghar, F. Li, Y. Zhou, Y. Wu, Z. Yu, S. Li, D. Tang, X. Han, J. Shang, Y. Liu, R.-W. Li, *Adv. Mater. Technol.* **2020**, *5*, 1900934.
[44] X. Hou, S. Zhang, J. Yu, M. Cui, J. He, L. Li, X. Wang, X. Chou, *Energy Technol.* **2020**, *8*, 1901242.
[45] J. Yu, X. Hou, J. He, M. Cui, C. Wang, W. Geng, J. Mu, B. Han, X. Chou, *Nano Energy* **2020**, *69*, 104437.
[46] A. Berns, U. Buder, E. Obermeier, A. Wolter, A. Leder, *Sens. Actuators, A* **2006**, *132*, 104.
[47] S. S. Kumar, A. K. Ojha, B. D. Pant, *Microsyst. Technol.* **2016**, *22*, 83.
[48] C. Hou, B. Wang, V. Murugadoss, S. Vupputuri, Y. Chao, Z. Guo, C. Wang, W. Du, *Eng. Sci.* **2020**, *11*, 19.
[49] Y. Ma, X. Xie, W. Yang, Z. Yu, X. Sun, Y. Zhang, X. Yang, H. Kimura, C. Hou, Z. Guo, W. Du, *Adv. Compos. Hybrid Mater.* **2021**, *4*, 906.
[50] H. Jing, L. Xu, X. Wang, Y. Liu, J. Hao, *J. Mater. Chem. A* **2021**, *9*, 19914.
[51] S.-H. Byun, J. Y. Sim, Z. Zhou, J. Lee, R. Qazi, M. C. Walicki, K. E. Parker, M. P. Haney, S. H. Choi, A. Shon, G. B. Gereau, J. Bilbily, S. Li, Y. Liu, W.-H. Yeo, J. G. McCall, J. Xiao, J.-W. Jeong, *Sci. Adv.* **2019**, *5*, eaay0418.
[52] M. D. Dickey, *Adv. Mater.* **2017**, *29*, 1606425.
[53] S.-H. Byun, J. Y. Sim, K.-C. Agno, J.-W. Jeong, *Mater. Today Adv.* **2020**, *7*, 100089.
[54] T. Xu, W. Wang, X. Bian, X. Wang, X. Wang, J. K. Luo, S. Dong, *Sci. Rep.* **2015**, *5*, 12997.
[55] M. S. Jokandan, F. Ajalloueian, M. Edinger, P. R. Stubbe, S. Baldursdottir, I. S. Chronakis, *J. Mech. Behav. Biomed. Mater.* **2018**, *79*, 92.
[56] C. F. Guimarães, L. Gasperini, A. P. Marques, R. L. Reis, *Nat. Rev. Mater.* **2020**, *5*, 351.
[57] J. Li, R. Bao, J. Tao, Y. Peng, C. Pan, *J. Mater. Chem. C* **2018**, *6*, 11878.
[58] H. Tian, Y. Shu, X.-F. Wang, M. A. Mohammad, Z. Bie, Q.-Y. Xie, C. Li, W.-T. Mi, Y. Yang, T.-L. Ren, *Sci. Rep.* **2015**, *5*, 8603.
[59] D. H. Kim, Y. Jung, K. Jung, D. H. Kwak, D. M. Park, M. G. Shin, H. J. Tak, J. S. Ko, *Micro Nano Syst. Lett.* **2020**, *8*, 24.
[60] W. Cheng, J. Wang, Z. Ma, K. Yan, Y. Wang, H. Wang, S. Li, Y. Li, L. Pan, Y. Shi, *IEEE Electron Device Lett.* **2018**, *39*, 288.
[61] S. Gong, W. Schwalb, Y. Wang, Y. Chen, Y. Tang, J. Si, B. Shirinzadeh, W. Cheng, *Nat. Commun.* **2014**, *5*, 3132.
[62] L. Qiu, M. Bulut Coskun, Y. Tang, J. Z. Liu, T. Alan, J. Ding, V.-T. Truong, D. Li, *Adv. Mater.* **2016**, *28*, 194.
[63] S. C. B. Mannsfeld, B. C.-K. Tee, R. M. Stoltenberg, C. V. H.-H. Chen, S. Barman, B. V. O. Muir, A. N. Sokolov, C. Reese, Z. Bao, *Nat. Mater.* **2010**, *9*, 859.
[64] L. Pan, A. Chortos, G. Yu, Y. Wang, S. Isaacson, R. Allen, Y. Shi, R. Dauskardt, Z. Bao, *Nat. Commun.* **2014**, *5*, 3002.
[65] M. Amjadi, K.-U. Kyung, I. Park, M. Sitti, *Adv. Funct. Mater.* **2016**, *26*, 1678.
[66] J. I. Yoon, K. S. Choi, S. P. Chang, *Microelectron. Eng.* **2017**, *179*, 60.
[67] Z. Kožíšek, P. Demo, *IOP Conf. Ser.: Mater. Sci. Eng.* **2017**, *266*, 012006.
[68] S.-H. Byun, C. S. Kim, K.-C. Agno, S. Lee, Z. Li, B. J. Cho, J.-W. Jeong, *Adv. Mater.* **2021**, *33*, 2007239.
[69] Y. Yang, Z. Liu, R. Jiang, R. Li, X. Li, *J. Alloys Compd.* **2019**, *811*, 151991.
[70] C. Zhang, L. Li, X. Yang, J. Shi, L. Gui, J. Liu, *Int. J. Heat Mass Transfer* **2020**, *148*, 119055.
[71] M. R. Khan, C. B. Eaker, E. F. Bowden, M. D. Dickey, *Proc. Natl. Acad. Sci. USA* **2014**, *111*, 14047.
[72] T. Shao, J. Wu, Y. Zhang, Y. Cheng, Z. Zuo, H. Lv, M. Ying, C. P. Wong, Z. Li, *Adv. Mater. Technol.* **2020**, *5*, 2000032.
[73] J. Wang, R. Suzuki, M. Shao, F. Gillot, S. Shiratori, *ACS Appl. Mater. Interfaces* **2019**, *11*, 11928.
[74] S. Park, H. Kim, M. Vosgueritchian, S. Cheon, H. Kim, J. H. Koo, T. R. Kim, S. Lee, G. Schwartz, H. Chang, Z. Bao, *Adv. Mater.* **2014**, *26*, 7324.
[75] J. Lee, J. Kim, Y. Shin, I. Jung, *Composites, Part B* **2019**, *177*, 107364.
[76] H. Kim, G. Kim, T. Kim, S. Lee, D. Kang, M.-S. Hwang, Y. Chae, S. Kang, H. Lee, H.-G. Park, W. Shim, *Small* **2018**, *14*, 1703432.
[77] K. Ha, W. Zhang, H. Jang, S. Kang, L. Wang, P. Tan, H. Hwang, N. Lu, *Adv. Mater.* **2021**, *33*, 2103320.
[78] Y. Wan, Z. Qiu, Y. Hong, Y. Wang, J. Zhang, Q. Liu, Z. Wu, C. F. Guo, *Adv. Electron. Mater.* **2018**, *4*, 1700586.
[79] F. Liu, F. Han, L. Ling, J. Li, S. Zhao, T. Zhao, X. Liang, D. Zhu, G. Zhang, R. Sun, D. Ho, C.-P. Wong, *Chem. - Eur. J.* **2018**, *24*, 16823.
[80] Z. He, W. Chen, B. Liang, C. Liu, L. Yang, D. Lu, Z. Mo, H. Zhu, Z. Tang, X. Gui, *ACS Appl. Mater. Interfaces* **2018**, *10*, 12816.
[81] C. G. Núñez, W. T. Navaraj, E. O. Polat, R. Dahiya, *Adv. Funct. Mater.* **2017**, *27*, 1606287.
[82] W. Cheng, L. Yu, D. Kong, Z. Yu, H. Wang, Z. Ma, Y. Wang, J. Wang, L. Pan, Y. Shi, *IEEE Electron Device Lett.* **2018**, *39*, 1069.
[83] S. Wan, H. Bi, Y. Zhou, X. Xie, S. Su, K. Yin, L. Sun, *Carbon* **2017**, *114*, 209.
[84] Y. Joo, J. Yoon, J. Ha, T. Kim, S. Lee, B. Lee, C. Pang, Y. Hong, *Adv. Electron. Mater.* **2017**, *3*, 1600455.
[85] S.-Y. Liu, J.-G. Lu, H.-P. D. Shieh, *IEEE Sens. J.* **2018**, *18*, 1870.
[86] D. Kwon, T.-I. Lee, M. S. Kim, S. Kim, T.-S. Kim, I. Park, in *2015 Transducers – 2015 18th Int. Conf. Solid-State Sensors, Actuators Microsystems (TRANSDUCERS)*, IEEE, Piscataway, NJ, USA **2015**, pp. 299–302.
[87] H. Shi, M. Al-Rubaiai, C. M. Holbrook, J. Miao, T. Pinto, C. Wang, X. Tan, *Adv. Funct. Mater.* **2019**, *29*, 1809116.
[88] J. Kim, E.-F. Chou, J. Le, S. Wong, M. Chu, M. Khine, *Adv. Healthcare Mater.* **2019**, *8*, 1900109.
[89] N. Wu, B. Zhao, J. Liu, Y. Li, Y. Chen, L. Chen, M. Wang, Z. Guo, *Adv. Compos. Hybrid Mater.* **2021**, *4*, 707.
[90] K. I. Kasozi, N. E. Mbiydzneyuy, S. Namubiru, A. A. Safiriyu, S. O. Sulaiman, A. O. Okpanachi, H. I. Ninsiima, *Afr. Health Sci.* **2018**, *18*, 828.
[91] Y. Tojo, N. Asamura, H. Shinoda, in *Proc. 41st SICE Annu. Conf. SICE 2002*, IEEE, Piscataway, NJ, USA **2002**, pp. 3205–3207.